

**Manuscript version: Author's Accepted Manuscript**

The version presented in WRAP is the author's accepted manuscript and may differ from the published version or Version of Record.

**Persistent WRAP URL:**

<http://wrap.warwick.ac.uk/166148>

**How to cite:**

Please refer to published version for the most recent bibliographic citation information. If a published version is known of, the repository item page linked to above, will contain details on accessing it.

**Copyright and reuse:**

The Warwick Research Archive Portal (WRAP) makes this work by researchers of the University of Warwick available open access under the following conditions.

Copyright © and all moral rights to the version of the paper presented here belong to the individual author(s) and/or other copyright owners. To the extent reasonable and practicable the material made available in WRAP has been checked for eligibility before being made available.

Copies of full items can be used for personal research or study, educational, or not-for-profit purposes without prior permission or charge. Provided that the authors, title and full bibliographic details are credited, a hyperlink and/or URL is given for the original metadata page and the content is not changed in any way.

**Publisher's statement:**

Please refer to the repository item page, publisher's statement section, for further information.

For more information, please contact the WRAP Team at: [wrap@warwick.ac.uk](mailto:wrap@warwick.ac.uk).

# Selective electroreduction of CO<sub>2</sub> and CO to C<sub>2</sub>H<sub>4</sub> by synergistically tuning nanocavities and surface charge of copper oxide

*Xin Li <sup>a</sup>, Lifan Li <sup>b</sup>, Qineng Xia <sup>b</sup>, Song Hong <sup>a</sup>, Leiduan Hao <sup>a</sup>, A. W. Robertson <sup>c</sup>, Hao Zhang <sup>d</sup>,  
Tsz Woon Benedict Lo <sup>d</sup>, Zhenyu Sun <sup>a\*</sup>*

<sup>a</sup> State Key Laboratory of Organic-Inorganic Composites, Beijing University of Chemical Technology, Beijing 100029, P. R. China. E-mail: sunzy@mail.buct.edu.cn

<sup>b</sup> College of Biological, Chemical Science and Engineering, Jiaxing University, Jiaxing, Zhejiang 314001, P. R. China

<sup>c</sup> Department of Physics, University of Warwick, Coventry CV4 7AL, U. K.

<sup>d</sup> Department of Applied Biology and Chemical Technology, The Hong Kong Polytechnic University, Hong Kong 621010, P. R. China

**KEYWORDS:** CO<sub>2</sub> reduction; CO reduction; Electrocatalysis; C<sub>2</sub>H<sub>4</sub>

**ABSTRACT:** Electroreduction of CO<sub>2</sub> and CO to high-value chemicals and fuels continues to be a grand challenge. Here we report synergistic electrolysis of CO<sub>2</sub> and CO to C<sub>2</sub>H<sub>4</sub> by concurrently tuning nanocavities and the interface of CuO with a hydrogen evolution inactive metal oxide (ZrO<sub>2</sub>). The designed CuO@ZrO<sub>2</sub> delivers a faradaic efficiency (FE) as high as 54.7 ± 1.1% towards C<sub>2</sub>H<sub>4</sub> formation and a remarkable overall CO<sub>2</sub> reduction FE exceeding 84.0% at 250 mA cm<sup>-2</sup>, significantly outperforming pristine CuO and many recently demonstrated Cu-based catalysts. The composite also exhibits a markedly enhanced FE of converting CO to C<sub>2</sub>H<sub>4</sub>, approximately three-fold that of pure CuO. Operando Raman spectroscopy as well as post-mortem XPS measurements verify that Cu<sup>+</sup> species are well retained in the presence of ZrO<sub>2</sub> during CO<sub>2</sub> reduction, in stark contrast to rapid transformation of Cu<sup>+</sup> to Cu<sup>0</sup> in the catalyst without the metal

oxide. Experiments in combination with theoretical calculations further show that the incorporation of  $\text{ZrO}_2$  substantially decreases the dimerization barriers of adsorbed CO intermediates, thus boosting C–C coupling to produce  $\text{C}_2\text{H}_4$ .

## INTRODUCTION

The levels of atmospheric  $\text{CO}_2$  continue to increase reaching 418.2 ppm (parts per million) in January 2022. This means irreversible and disruptive consequences to our climate and environment. Electrochemical  $\text{CO}_2$  reduction (ECR) to fuels or commodity chemicals driven by renewably generated electricity offers a potential strategy to ameliorate greenhouse effect, enabling carbon fixation and energy storage for intermittent renewables.<sup>1-10</sup> Among different products, ethylene ( $\text{C}_2\text{H}_4$ ) is an industrial feedstock (for polyethylene) that is in high demand. It is also widely utilized in agriculture to accelerate fruit ripening.<sup>5</sup> However, it remains challenging to attain efficient ECR to  $\text{C}_2\text{H}_4$  due to 1) the competitive undesirable  $\text{H}_2\text{O}$  (or proton) reduction reaction; 2) the high energy of the C–C bond and the competitive formation of C–H, C–O, and C–C bonding; and 3) the large overpotential difference between the generation of essential CO species and that of the  $\text{C}_2$  moieties.<sup>11-13</sup> To facilitate the preferential transformation of  $\text{CO}_2$  to  $\text{C}_2\text{H}_4$ , prior reports have focused on modification of Cu catalysts through heteroatom alloying,<sup>16</sup> doping,<sup>14,15</sup> or manipulation of facets,<sup>17</sup> oxidation state,<sup>18</sup> and surface structure.<sup>19</sup> However,  $\text{C}_2\text{H}_4$  production via ECR still suffers from low efficiency and selectivity. To circumvent these issues, the preparation and tailoring of synergistic catalytic materials that enable both inhibition of the unwanted hydrogen evolution reaction (HER) and enhancement of  $\text{CO}_2$  activation and C–C coupling is highly desirable.<sup>20,21</sup>

The exact reaction mechanism for  $C_2H_4$  formation from ECR is still under debate. Three major protocols have been put forth: 1) “carbene” mechanism; 2)  $*CO$  dimerization ( $*$  denotes the adsorbed intermediate); and 3) coupling of  $CHO^*$  (with  $*CO$  or  $CHO^*$ ).<sup>13,22</sup> For the carbene mechanism, hydroxycarbene or carbenes are generated and then reduced to  $*CH_2$  species. Further reaction of two  $*CH_2$  moieties or insertion of  $CO$  in  $*CH_2$  following a Fischer Tropsch-type manner gives rise to  $C_2H_4$ . Alternatively,  $C_2H_4$  can be formed through dimerization of  $*CO$  intermediates, which is proposed to be a critical step for C–C bond formation at low overpotentials.<sup>22</sup> Two  $*CO$  species couple to yield  $*C_2O_2$  which is consecutively hydrated to  $*CO-COH$ . Vinyl alcohol ( $*CH_2-CHO$ ) is then formed and further transformed into  $C_2H_4$ . Under high overpotentials  $*CO$  is predicted to first reduce to  $*CHO$ , then subsequently couple with  $*CO$  to generate  $*COCHO$ , being more preferable than  $*CO$  dimerization and reduction.<sup>22</sup>  $C_2H_4$  is obtained via the subsequent formation and reduction of  $*COCHOH$ . In an alternative pathway, two  $CHO^*$  species couple to form  $OHC-CHO^*$  which converts to  $*CH_2CHO$  and is further reduced to ethylene oxide ( $CH_2CH_2O^*$ ).  $C_2H_4$  can then be produced either through direct breaking of C–O bond in  $CH_2CH_2O^*$  or via hydrogenation to  $CH_3CH_2OH^*$ .

Regardless of the operational mechanism,  $*CO$  is the common intermediate for the production of  $C_2H_4$  and other  $C_{2+}$  products. From this scenario, optimizing the coverage and coupling of the  $*CO$  intermediate and simultaneously inhibiting undesirable H adsorption are key to boosting  $CO_2$  (and  $CO$ ) reduction selectively to  $C_2H_4$ . In addition,  $Cu^+$  is supposed to strengthen  $*CO$  adsorption (because of the availability of vacant 3d orbitals) to further boost C–C coupling by lowering the Gibbs free energy for  $*OCCOH$  formation. Nevertheless,  $Cu^+$  moieties tend to be reduced under ECR environment,<sup>13</sup> resulting in metallic  $Cu$  that may

deteriorate the C<sub>2+</sub> formation. Under such circumstance, stabilization of Cu<sup>+</sup> species during CO<sub>2</sub> reduction is key. In this work, we seek to explore a synergistic effect by introducing nanoholes and tailoring the interface between CuO and a second component. The porosity of the catalyst favours diffusion of CO<sub>2</sub> to copper sites, thereby significantly increasing the availability of each catalytic center. ZrO<sub>2</sub> is selected as the second phase to create an intimate interface by virtue of its low cost, high surface basicity and good CO<sub>2</sub> adsorption capacity, and outstanding thermal and chemical stability. Meanwhile, ZrO<sub>2</sub> can mitigate the HER.<sup>23</sup> In addition to these benefits, we find that incorporation of the reducible metal oxide can stabilize Cu<sup>+</sup>, as validated by operando Raman spectroscopy, X-ray photoelectron spectroscopy (XPS), and further Bader charge analysis. Such a strategy allows us to readily regulate \*CO availability on copper sites, enabling high selectivity to C<sub>2</sub>H<sub>4</sub> at large production rates. The ZrO<sub>2</sub> promoted Cu surfaces deliver an FE close to 48% and a cathodic energy efficiency (EE) of ~26.8% towards C<sub>2</sub>H<sub>4</sub> formation in an H-type cell. This represents a substantial improvement, outperforming each component alone and many recently reported electrocatalysts. Furthermore, the overall FE and FE for C<sub>2</sub>H<sub>4</sub> can be further improved up to 84.3 ± 1.6% and 54.7 ± 1.1%, respectively under a high current density of 250 mA cm<sup>-2</sup> using a flow reactor. The role of ZrO<sub>2</sub> was also investigated by density functional theory (DFT) modeling, which illustrated a substantially boosted C–C coupling of \*CO, thus accelerating C<sub>2</sub>H<sub>4</sub> formation.

## RESULTS AND DISCUSSION

A facile wet chemical synthesis scheme was used here to fabricate CuO@ZrO<sub>2</sub> composites with adjustable composition. X-ray diffraction patterns (XRD) measurements confirmed the

yield of highly crystalline CuO and ZrO<sub>2</sub>. Those diffraction peaks at ~23.9, 28, 31.3, 34, 40.5, 45.3, and 49° can be well assigned to the (011), ( $\bar{1}11$ ), (111), (002), (211), (202), and (220) reflections of monoclinic ZrO<sub>2</sub> (JCPDS no.: 74–0815) respectively, while the peaks at around 35.5, 38.7, 48.7, 61.5, and 68° correspond to the ( $\bar{1}11$ ), (111), ( $\bar{2}02$ ), ( $\bar{1}13$ ), and (220) planes of monoclinic CuO (JCPDS no.: 80–1916) (Fig. 1a and Fig. S1). Note that no typical peaks ascribed to reflections of CuZrO<sub>3</sub> (JCPDS no.: 43–0953) were discernible, thus ruling out the formation of the mixed metal oxide.

XPS analysis was performed to probe the chemical composition of the surface and sub-surface (up to a depth of 5 nm) of the samples. The wide-survey XPS spectrum reveals the spectroscopic characters of Cu, O, and Zr (Fig. S2a). No other heteroelements including element Cl were detected, indicating the absence of impurities, unreacted precursors or by-products in the sample. Shown in Fig. 1b are the Cu 2p XPS spectra of pristine CuO and CuO@ZrO<sub>2</sub>. The Cu 2p peaks of CuO@ZrO<sub>2</sub> were observed to shift to smaller electron binding energies (BEs) relative to bare CuO, which signifies that the electron charge density around Cu became richer after introduction of ZrO<sub>2</sub>. A spin-orbit split doublet with Cu 2p<sub>1/2</sub> at 953.7 eV and 2p<sub>3/2</sub> at 933.8 eV for both CuO and CuO@ZrO<sub>2</sub> mainly originates from Cu<sup>2+</sup> species.<sup>24</sup> Three characteristic Cu<sup>2+</sup> satellites at 961.5, 943, and 940.6 eV were also seen. The deconvoluted Cu 2p<sub>1/2</sub> at 951.9 eV and 2p<sub>3/2</sub> at 932.2 eV suggest the presence Cu<sup>+</sup> moieties.<sup>25</sup> The LMM Auger excitation spectra of Cu (Fig. 1c) confirmed the existence of Cu<sup>+</sup> in CuO@ZrO<sub>2</sub> which is however not the case for pristine CuO. The intense peak at 568.5 eV can be unambiguously assigned to Cu<sup>2+</sup>, while the Auger peak at ~570 eV arises from Cu<sup>+</sup>. The peak at 574.5 eV represents distinct Auger transitions associated with Cu<sup>+</sup>.<sup>17</sup> No apparent Cu<sup>0</sup> signal, supposed at ~568 eV, was identified. The O 1s spectra can be deconvoluted into three

sub-bands (Fig. S2b). The signal at about 533.1 eV stems from the surface –OH groups.<sup>26</sup> The other two oxygen peaks at ~530.5 and 529.5 eV arise respectively from vacancy oxygen and lattice oxygen.<sup>14,27</sup> The vacancy oxygen-to-lattice oxygen ratio in CuO@ZrO<sub>2</sub> approximates about 0.58, considerably exceeding the value of ~0.21 for neat CuO and ~0.19 for pure ZrO<sub>2</sub>. The increase in oxygen vacancy sites tends to assist in CO<sub>2</sub> adsorption and activation. The two strong peaks with BEs at 181.6 and 184.0 eV are associated with Zr 3d<sub>3/2</sub> and 3d<sub>5/2</sub> of Zr<sup>4+</sup> in the composite (Fig. S2c).<sup>28</sup> The BE value of Zr 3d<sub>5/2</sub> was found to be about 0.3 eV higher than that of bare ZrO<sub>2</sub>, demonstrating electron transfer from Zr to Cu, in agreement with the result observed for Cu.

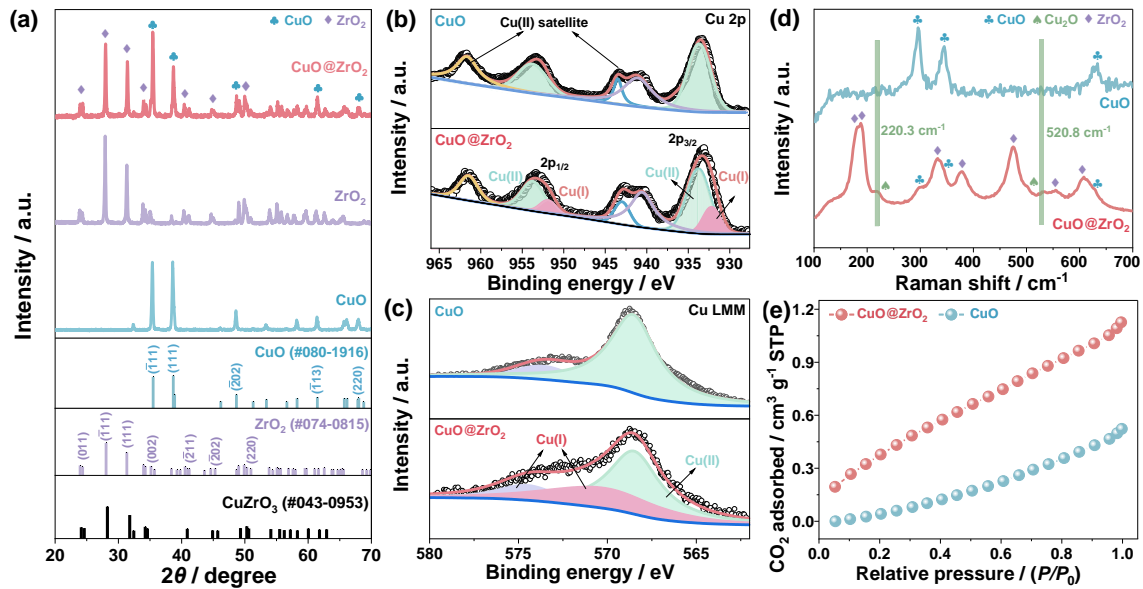


**Fig. 1.** (a) XRD patterns of CuO, ZrO<sub>2</sub>, and CuO@ZrO<sub>2</sub>. (b) Cu 2p and (c) Cu LMM Auger XPS spectra, (d) Raman spectra, and (e) CO<sub>2</sub> desorption isotherms of CuO and CuO@ZrO<sub>2</sub>.

Raman spectroscopy was employed to probe the local atomic structures and vibrations of CuO@ZrO<sub>2</sub>. The signals at 189, 476, and 562 cm<sup>-1</sup> can be attributed to the A<sub>g</sub> modes while the peaks at 322, 380, and 608 cm<sup>-1</sup> are associated with the B<sub>g</sub> modes of monoclinic ZrO<sub>2</sub>

(Fig. 1d)<sup>29</sup>. Another distinct peak at 179 cm<sup>-1</sup> is likely the A<sub>g</sub> + B<sub>g</sub> mode of ZrO<sub>2</sub>. Three one-phonon vibrations at 290.6, 345.2, and 626.7 cm<sup>-1</sup> were observed for both pure CuO and CuO@ZrO<sub>2</sub>, corresponding to the A<sub>g</sub> mode and two B<sub>g</sub> optical modes of cupric oxide.<sup>14</sup> Moreover, two additional peaks at ~220.3 and 520.8 cm<sup>-1</sup> were discernible for CuO@ZrO<sub>2</sub> that can be ascribed to the Cu<sup>+</sup> species in the composite,<sup>18</sup> in accord with the aforementioned XPS results.

Temperature-programmed reduction by hydrogen (H<sub>2</sub>-TPR) measurements present two major peaks at ~200 and 325 °C (Fig. S3), which are associated with the respective stepwise reduction of Cu<sup>2+</sup> to Cu<sup>+</sup> and Cu<sup>+</sup> to Cu<sup>0</sup> by removing reducible oxygen from the CuO<sub>x</sub> species in CuO@ZrO<sub>2</sub>. Note that the reduction temperatures obviously decreased compared to pure CuO, which may result from H<sub>2</sub> spillover to CuO at the CuO@ZrO<sub>2</sub> interface. This suggests that adjacent ZrO<sub>2</sub> can help reduce CuO<sub>x</sub> in the composite. Equally importantly, CuO@ZrO<sub>2</sub> possesses a CO<sub>2</sub> uptake of ~2.2 mg<sub>CO2</sub> g<sub>cat.</sub><sup>-1</sup> at 1 atmospheric pressure and 298.15 K (Fig. 1e), 2.2 fold as large as that of bare CuO, which is mostly attributed to the high CO<sub>2</sub> adsorption capacity of ZrO<sub>2</sub> via carbonate formation. This undoubtedly favours enrichment of CO<sub>2</sub> on the local surface of the cathode and potentially promotes catalytic turnover.

To decipher the morphology and microstructure of the as-made materials, scanning electron microscopy (SEM), transmission electron microscopy (TEM) and high-angle annular dark-field scanning transmission electron microscopy (HAADF-STEM) were adopted. Despite of the varied Cu/Zr ratios, CuO@ZrO<sub>2</sub> catalysts display a capsule-like shape with lateral sizes of ~500 nm (Figs. 2a and b, and S4). Energy-dispersive X-ray spectroscopy (EDS) elemental mapping (Fig. 2c-f), with the corresponding spectrum (Fig. 2g), demonstrated the prevalence and uniform dispersion of Zr, Cu, and O elements throughout the sample, pointing to the



intimate contact between the two metal oxides. Interestingly, several pits on the surface of  $\text{CuO@ZrO}_2$  were vividly observed by STEM (Fig. 2h and i, Fig. S5a and b). Higher magnification HAADF-STEM images (Fig. S5a, false color Fig. S5b) reveal that some pits are less than 5 nm in diameter, and are more clearly resolvable at the thinner edges of the capsule. High-resolution TEM observation (Fig. 2j) along with fast Fourier transformation (FFT) (Fig. 2k and l) indicates good crystallinity of the  $\text{CuO@ZrO}_2$ . Ordered lattice fringes with an interplanar spacing of  $\sim 3.2$  and  $2.7$  Å are clearly seen corresponding to the ( $\bar{1}11$ ), ( $1\bar{1}0$ ) planes of  $\text{ZrO}_2$  and  $\text{CuO}$ .<sup>30</sup>

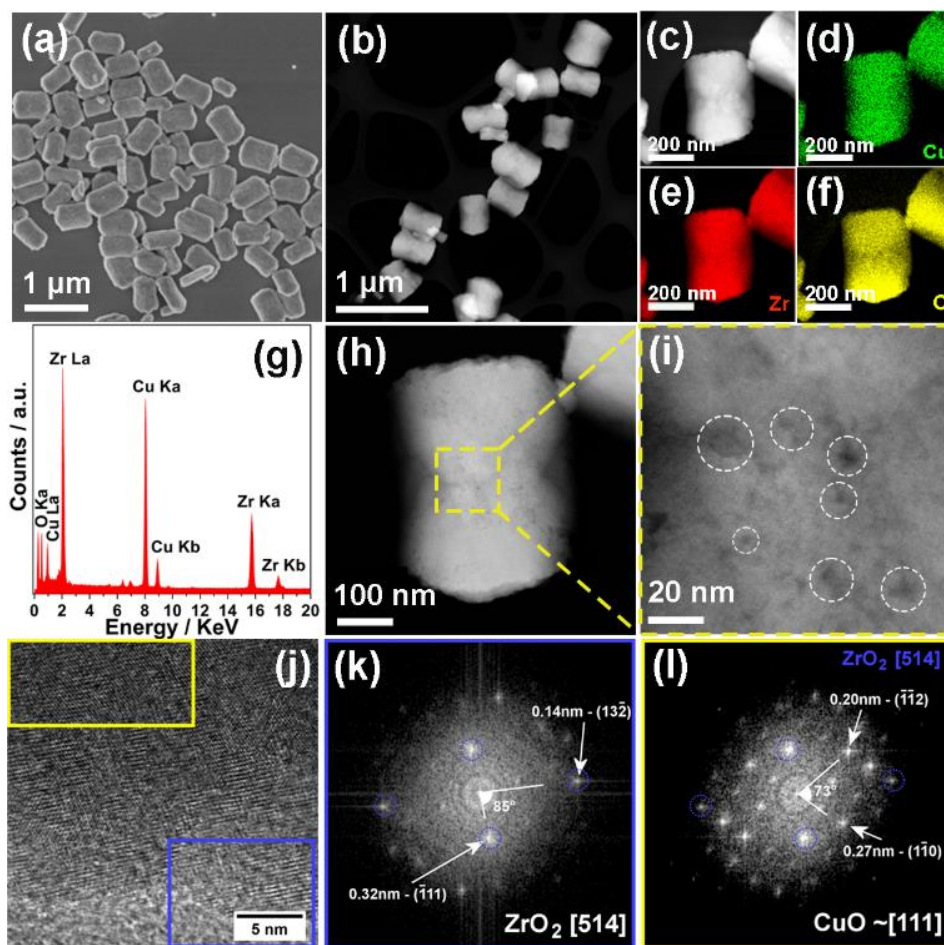


**Fig. 2.** (a) SEM and (b) low-magnification STEM images, and (c) STEM image and corresponding EDS elemental maps of (d) Cu, (e) Zr, (f) O, and (g) EDS spectrum of CuO@ZrO<sub>2</sub>. (h and i) HAADF-STEM images. (j) High-resolution TEM image of CuO@ZrO<sub>2</sub>. (k) and (l) FFTs of the areas encased by the blue and yellow rectangles in (j), respectively.

The intrinsic catalytic properties of the as-obtained CuO@ZrO<sub>2</sub> were evaluated for ECR in an air-tight H-type cell with two cathodic and anodic compartments which are separated by using a Nafion 117 membrane with continuous CO<sub>2</sub> flow.<sup>31</sup> All voltages applied are referred to the reversible hydrogen electrode (RHE) reference unless specified otherwise. Larger reduction current densities were achieved under a CO<sub>2</sub> environment than in an Ar atmosphere across the potential regions (Fig. 3a). At voltages being more negative than −0.6 V, the reduction current increases abruptly in CO<sub>2</sub>-saturated 0.1 M KHCO<sub>3</sub> solution, possibly resulting from the occurrence of intense CO<sub>2</sub> reduction. The gas and liquid products were quantified by gas chromatography (GC) and proton nuclear magnetic resonance (<sup>1</sup>H NMR), respectively.<sup>32</sup>

CO, H<sub>2</sub>, HCOOH, CH<sub>4</sub>, and C<sub>2</sub>H<sub>4</sub> were produced between −0.8 to −1.3 V over both CuO and CuO@ZrO<sub>2</sub> catalysts, whereas only minor amounts of HCOOH were attained on ZrO<sub>2</sub> (Fig. 3b). CO and HCOOH comprise the major ECR products at potentials ≥ −0.8 V. With increase of overpotential, more CO was produced leading to higher \*CO coverage. C<sub>2</sub>H<sub>4</sub> was preferentially generated at potentials below −1.0 V. The overall ECR FE and the FE for C<sub>2</sub>H<sub>4</sub> formation show a volcano-type relationship with the increase of overpotential, reaching a maximum at −1.1 V. Note that both metrics are invariably higher for CuO@ZrO<sub>2</sub> than those on pure CuO in the entire potential range. This underscores the role of ZrO<sub>2</sub> in impeding HER and also promoting the further conversion of adsorbed \*CO to C<sub>2</sub>H<sub>4</sub> and \*CO protonation to

CH<sub>4</sub> (at more negative potentials). Especially, the CuO@ZrO<sub>2</sub> imparts an average maximum ECR FE of 68% and a C<sub>2</sub>H<sub>4</sub> FE of 47.6%, approximately 2.1 and 2.4 times that of pure CuO, respectively. Likewise, the highest partial C<sub>2</sub>H<sub>4</sub> geometric current density and C<sub>2</sub>H<sub>4</sub> production rate of CuO@ZrO<sub>2</sub> are ~5.4 mA cm<sup>-2</sup> and 13.9 μmol mg<sub>cat.</sub><sup>-1</sup> h<sup>-1</sup>, 2.3 and 2.5 fold that of individual CuO (Fig. 3c, d and Fig. S6). The partial C<sub>2</sub>H<sub>4</sub> current density of CuO@ZrO<sub>2</sub> normalized based on electrochemical active surface area (ECSA) as reflected by double-layer capacitance (*C<sub>dl</sub>*) (Fig. S7) is 2.3 times that of pure CuO. In addition, the selectivity of ECR to C<sub>2</sub>H<sub>4</sub> (FE<sub>C<sub>2</sub>H<sub>4</sub></sub>/FE<sub>total</sub>) on CuO@ZrO<sub>2</sub> is much greater than that on bare CuO over a wide potential window from -0.8 to -1.2 V (Fig. 3e). Evidently, the partial current density arising from HER is appreciably lessened after incorporation of ZrO<sub>2</sub> (Fig. 3f).

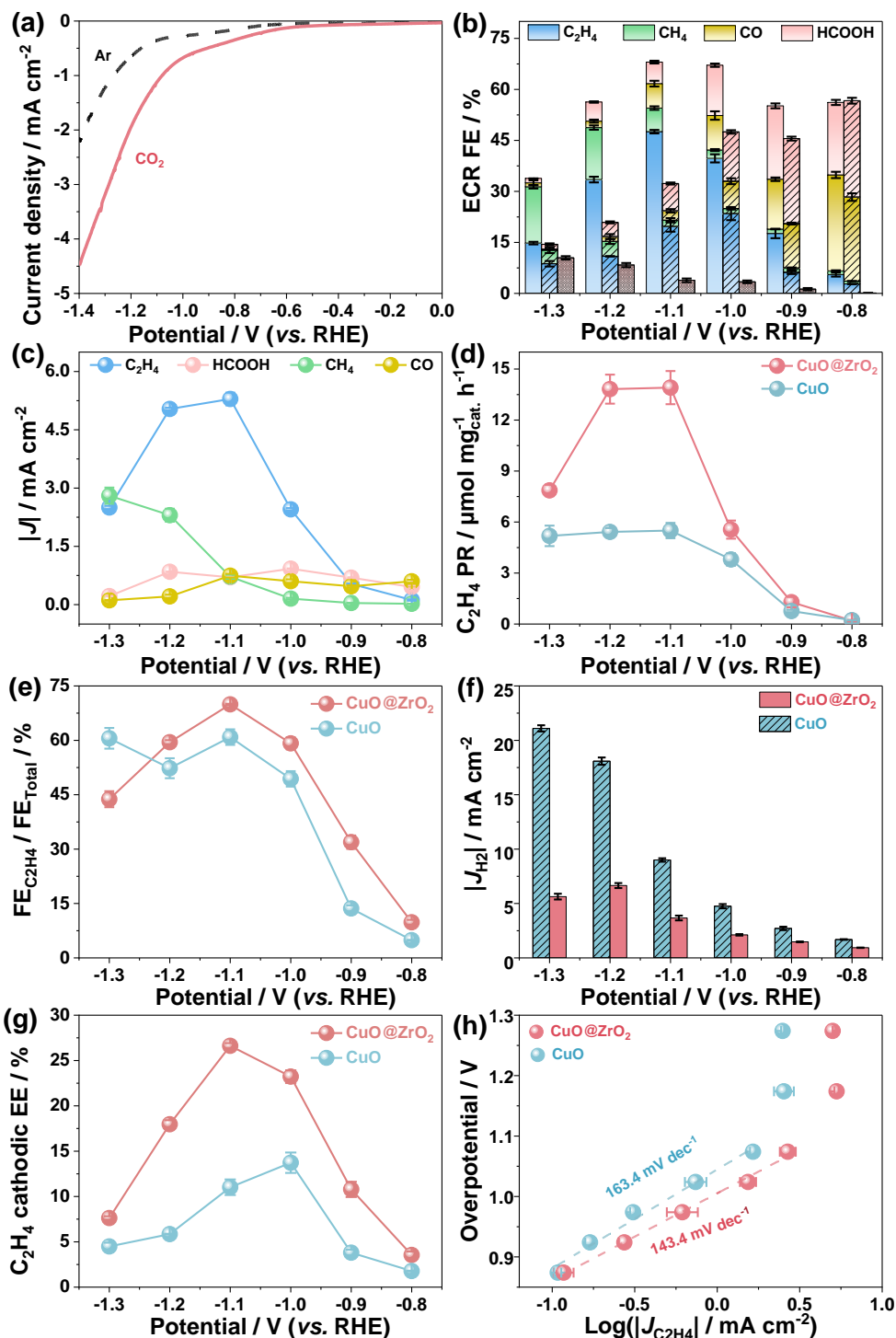


**Fig. 3.** (a) Linear sweep voltammetry (LSV) curves of CuO@ZrO<sub>2</sub> in 0.1 M KHCO<sub>3</sub> solution saturated with Ar (dashed line) or CO<sub>2</sub> (solid line). The sweep rate is 5 mV s<sup>-1</sup>. (b) ECR FE over bare CuO (striped column), ZrO<sub>2</sub> (dotted column), and CuO@ZrO<sub>2</sub>. (c) Partial geometric current

density for different ECR products over CuO@ZrO<sub>2</sub>. (d) C<sub>2</sub>H<sub>4</sub> production rate, (e) FE<sub>C<sub>2</sub>H<sub>4</sub></sub>/FE<sub>total</sub> ratio, (f) partial geometric current density for H<sub>2</sub> evolution, and (g) C<sub>2</sub>H<sub>4</sub> cathodic EE on CuO and CuO@ZrO<sub>2</sub> at various applied voltages. (h) Tafel plots for C<sub>2</sub>H<sub>4</sub> production together with corresponding fitting profiles over neat CuO and CuO@ZrO<sub>2</sub>.

Furthermore, we calculated the C<sub>2</sub>H<sub>4</sub> cathodic EE from the FE for C<sub>2</sub>H<sub>4</sub> formation and the ratio of the reaction thermodynamics over cell voltage:  $[EE = FE_{C_2H_4} \times (E^0_{O_2/H_2O} - E^0_{CO_2/C_2H_4}) / (E^0_{O_2/H_2O} - E^0_{CO_2/C_2H_4} + \eta_{cathodic})]$  (Eq. 1). The highest C<sub>2</sub>H<sub>4</sub> cathodic EE (26.8 ± 0.3%) was accomplished at 11.2 mA cm<sup>-2</sup> (Fig. 3g). Remarkably, the FE of C<sub>2</sub>H<sub>4</sub> on CuO@ZrO<sub>2</sub> even exceeds many recently reported Cu-based materials under comparable or larger overpotentials (Table S1), such as the state-of-the-art porous Cu (maximum C<sub>2</sub>H<sub>4</sub> FE: 35.8%),<sup>33</sup> Ag<sub>1</sub>-Cu<sub>1.1</sub> nanodimers (maximum C<sub>2</sub>H<sub>4</sub> FE: 40%),<sup>34</sup> and Cu/GDL (maximum C<sub>2</sub>H<sub>4</sub> FE: 40.2%)<sup>35</sup>. The C<sub>2</sub>H<sub>4</sub> EE of 26.8% at 11.2 mA cm<sup>-2</sup> also surpasses most previous results shown over Cu-based electrodes, as summarized in Table S1. Electrochemical impedance spectroscopy (EIS) measurements (Fig. S8) showed a slightly lower charge transfer resistance of CuO@ZrO<sub>2</sub> compared with pure CuO. This enables more facile electron exchange between the working electrode and reactants in the electrolyte, benefiting the ECR. Moreover, a Tafel slope of 143.4 mV dec<sup>-1</sup> was observed for CuO@ZrO<sub>2</sub>, lower than 163.4 mV dec<sup>-1</sup> for pure CuO (Fig. 3h). This indicates that the composite has a relatively faster reaction kinetics for ECR.

The ECR performance could be readily tailored by manipulation of the ratio of the two metal oxides. Increasing the content of ZrO<sub>2</sub> was observed to lead to a monotonic drop of CO FE (Fig. S9). This may be owing to the increased \*CO coverage and transformation induced by the incorporation of ZrO<sub>2</sub>. Both the overall ECR FE and C<sub>2</sub>H<sub>4</sub> FE increased upon improving the Zr/Cu molar ratio, reaching a peak value at the optimal dosage of 2:3 (Fig. 4).

Nonetheless, further increase of Zr content resulted in deterioration of the ECR performance. This is probably due to the reduction in both electrical conductivity and the number of Cu active sites for CO<sub>2</sub> activation. We also found that control of defects (e.g. pits) in CuO by regulating the additional amount of NaOH permits tuning of ECR activity. The overall ECR FE can be greatly augmented to about 68% for defective CuO@ZrO<sub>2</sub>, in contrast to that of 18.5% for a counterpart without defects (Fig. S9d). It is noteworthy that under equivalent electrochemical conditions, the overall ECR FE as well as C<sub>2</sub>H<sub>4</sub> selectivity over CuO@ZrO<sub>2</sub> are also dramatically superior than those of the commercial Cu, CuO, Cu<sub>2</sub>O, and Cu(OH)<sub>2</sub> (Fig. 4).

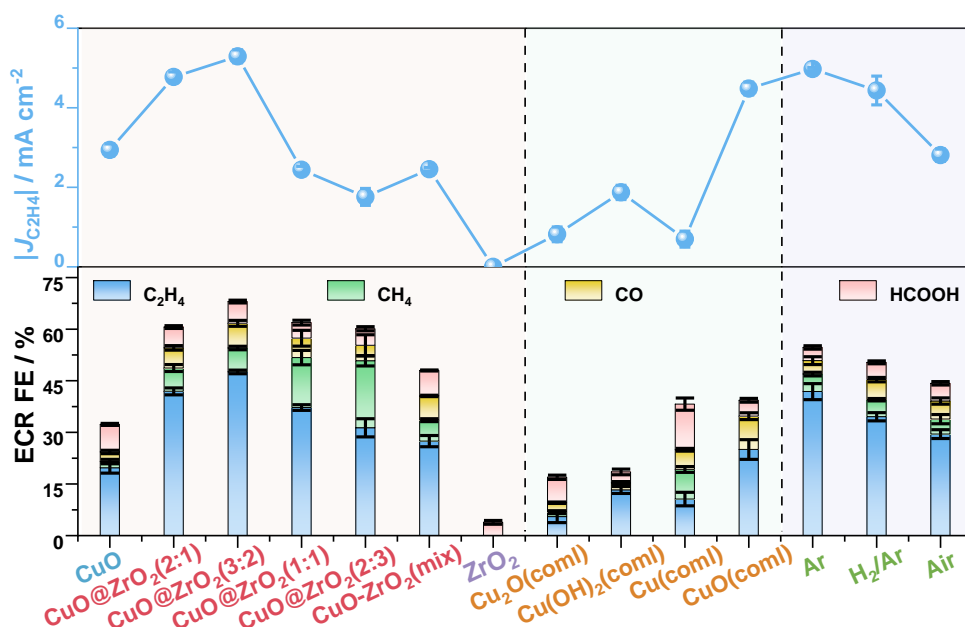


**Fig. 4.** C<sub>2</sub>H<sub>4</sub> partial geometric current density (upper panel) and FE (bottom panel) over CuO@ZrO<sub>2</sub> catalysts with varying Cu/Zr molar ratios, commercial (coml) Cu, Cu<sub>2</sub>O, CuO, Cu(OH)<sub>2</sub>, treated CuO@ZrO<sub>2</sub> in different atmospheres (Ar, 8% H<sub>2</sub>/Ar, and air) at 200 °C for 1 h, and also the pure CuO and ZrO<sub>2</sub> synthesized here at -1.1 V.

We further investigated the impact of  $\text{Cu}^+$  during ECR by annealing  $\text{CuO@ZrO}_2$  at 200 °C by exposure to distinct atmospheres (Fig. 4). The relative percentages of  $\text{Cu}^0$ ,  $\text{Cu}^+$ , and  $\text{Cu}^{2+}$  in the resultant catalysts were analyzed by XPS (Table S2 and Fig. S10). Treatment in Ar to convert a small fraction of  $\text{Cu}^{2+}$  to  $\text{Cu}^+$  and  $\text{Cu}^+$  to  $\text{Cu}^0$  (Table S2 and Fig. S10a) mildly degraded the ECR activity. The overall ECR FE and  $\text{C}_2\text{H}_4$  FE as well as partial current density all descended. Annealing the catalyst in 8%  $\text{H}_2/\text{Ar}$  resulted in a more pronounced drop in  $\text{C}_2\text{H}_4$  FE (to 34.5%). This may be attributed to the lessened  $\text{Cu}^+/\text{Cu}^0$  ratio (Table S2 and Fig. S10b) detrimental to C–C coupling. We also found that treatment of the sample in air at elevated temperatures substantially deteriorated the ECR performance especially the FE for  $\text{C}_2\text{H}_4$  production, whereas  $\text{H}_2$  evolution became more severe. This may be associated with the decrease in  $\text{Cu}^+/\text{Cu}^{2+}$  (Table S2 and Fig. S10c).

To verify the importance of the  $\text{CuO-ZrO}_2$  interface, we mediated the interfacial structure by controlling the feeding sequence of the two metal precursors during synthesis. When  $\text{Cu}(\text{Ac})_2$  and  $\text{ZrCl}_4$  were added separately to prepare the catalyst, the  $\text{C}_2\text{H}_4$  FE was markedly reduced (Table S3). In either case, the accessible  $\text{CuO-ZrO}_2$  interfaces with exposed copper sites were evidently diminished, thus leading to the declined ECR performance. Alternatively, individual  $\text{CuO}$  and  $\text{ZrO}_2$  were physically mixed as a control ( $\text{CuO/ZrO}_2\text{-mix}$ ) that has equivalent metal oxide contents with  $\text{CuO@ZrO}_2$ , which however gave inferior  $\text{CO}_2$  reduction activity (Fig. 4). This is likely owing to the reduced intimate  $\text{CuO-ZrO}_2$  interfaces and poor mass transport. Based on the above results, we propose that rational design of  $\text{CuO-ZrO}_2$  interfaces to facilitate and stabilize surface  $\text{Cu}^+$  species is vital to accelerate the  $\text{CO}_2$ -to- $\text{C}_2\text{H}_4$  transformation.

Cycling assays with alternated electrolysis between Ar- and CO<sub>2</sub>-purged solutions indicated that the C<sub>2</sub>H<sub>4</sub> FE remained essentially constant for at least 4 cycles (Fig. 5a). It also supported that the obtained C<sub>2</sub>H<sub>4</sub> was generated from the feed gas CO<sub>2</sub>. Strikingly, no obvious decay in C<sub>2</sub>H<sub>4</sub> current density and FE occurred even following continuous electrolysis for 12 h, reflecting considerable catalytic durability of CuO@ZrO<sub>2</sub> (Fig. 5b). Post characterization by XPS (Fig. S12a and b) manifested that the surface concentration of Cu<sup>+</sup> was largely maintained after electrolysis at −1.1 V, probably resulting from the strong interplay between ZrO<sub>2</sub> and CuO. In addition, the morphology and size of CuO@ZrO<sub>2</sub> after electrolysis were well preserved, further confirming its good stability (Fig. S11).

We further conducted operando Raman spectroscopy measurements to monitor the catalyst structural evolution in operando during the ECR (Fig. 5c and d). In the spectra measured at the open-circuit potential (OCP), both CuO@ZrO<sub>2</sub> and CuO display peaks at 290.6 and 345.2 cm<sup>−1</sup> ascribed to CuO. The additional peaks for CuO@ZrO<sub>2</sub> at ~380 and 476 cm<sup>−1</sup> correspond to ZrO<sub>2</sub>, whereas the signals at 220.3, 419.0, and 640.1 cm<sup>−1</sup> originate from Cu<sub>2</sub>O, associated with the respective 2Γ<sup>−</sup><sub>12</sub>, 4Γ<sup>−</sup><sub>12</sub>, and Γ<sup>−</sup><sub>12</sub> + Γ<sup>+</sup><sub>25</sub> modes.<sup>36</sup> Interestingly, the CuO@ZrO<sub>2</sub> retains the characteristic Raman modes of Cu<sub>2</sub>O within 60 minutes of CO<sub>2</sub> electrolysis (Fig. 5c), implying that the ZrO<sub>2</sub> can protect Cu<sup>+</sup> species from further reduction to a great extent. In sharp contrast, for the neat CuO catalyst, the Raman signals of CuO and Cu<sub>2</sub>O disappear rapidly after 10 minutes under the realistic operando conditions (Fig. 5d), indicating the full reduction of Cu<sup>2+</sup> to Cu<sup>0</sup>.



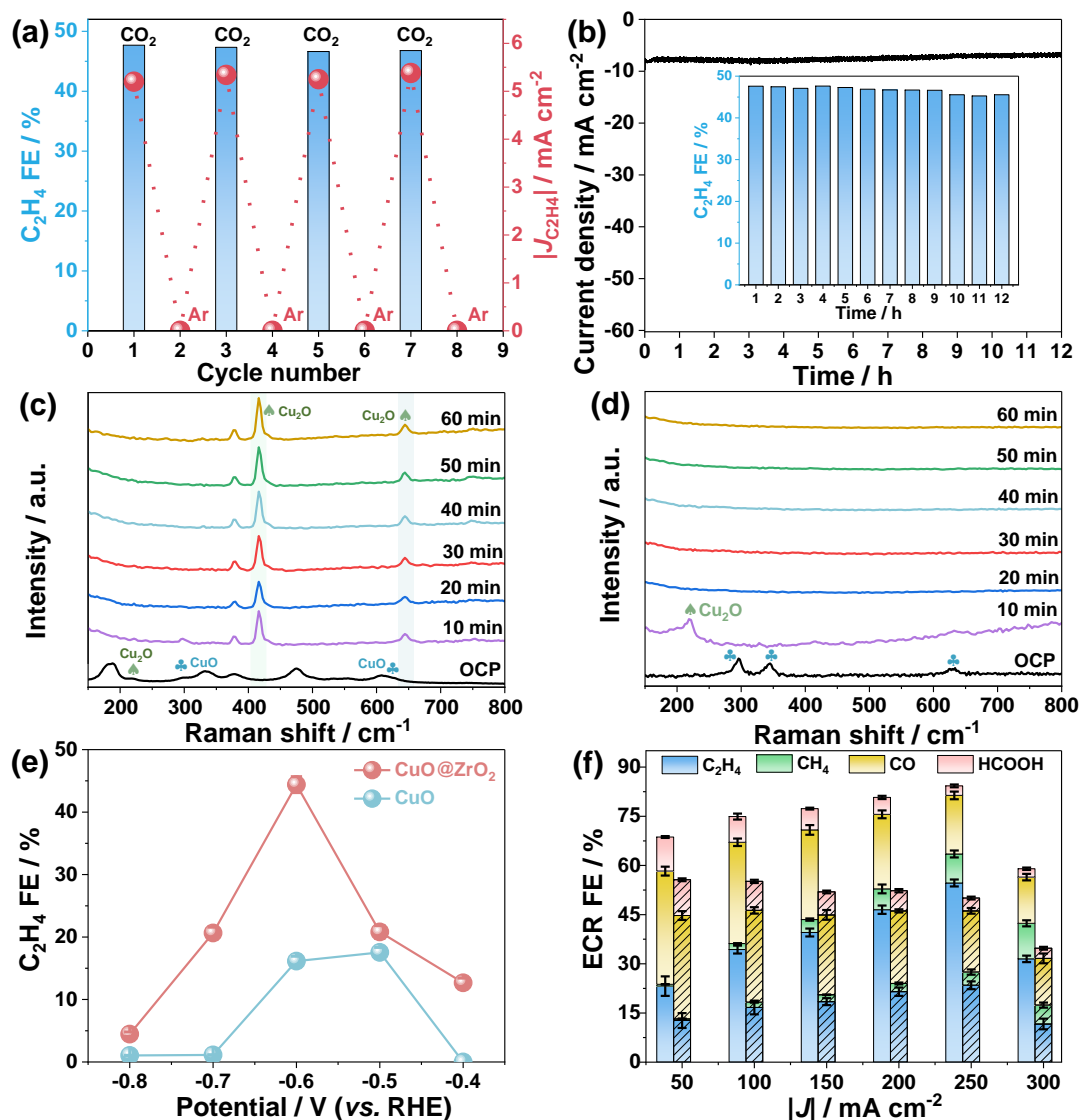


**Fig. 5.** (a) C<sub>2</sub>H<sub>4</sub> FE (bar) and corresponding partial geometric current density (ball) for CuO@ZrO<sub>2</sub> versus alternate cycles with an interval of 1 h in CO<sub>2</sub>- and Ar-purged 0.1 M KHCO<sub>3</sub> at -1.1 V. (b) Geometric current density- and C<sub>2</sub>H<sub>4</sub> FE (the inset) as a function of electrolysis time on CuO@ZrO<sub>2</sub> for ECR at -1.1 V. Operando Raman spectra of (c) CuO@ZrO<sub>2</sub> and (d) CuO at different ECR reaction times at -1.1 V. (e) FE for C<sub>2</sub>H<sub>4</sub> formation via the electrochemical CO reduction over bare CuO and CuO@ZrO<sub>2</sub> in 0.1 M KOH solutions purged with CO at ambient

temperature. (f) ECR FEs of CuO@ZrO<sub>2</sub> and bare CuO over the geometric current range from 50 to 300 mA cm<sup>-2</sup> in a flow cell with 1.0 M aqueous KOH as both catholyte and anolyte.

We found that CuO@ZrO<sub>2</sub> also enabled selective electroreduction of CO towards C<sub>2</sub>H<sub>4</sub>. The C<sub>2</sub> product started to form at a potential as low as -0.4 V which is rather unlikely for pure CuO. In the entire voltage range between -0.4 and -0.8 V, CuO@ZrO<sub>2</sub> showed superior C<sub>2</sub>H<sub>4</sub> formation efficiency with the maximum C<sub>2</sub>H<sub>4</sub> FE of 44.4 ± 1.3% at -0.6 V, being 2.5-fold that of pure CuO.

Due to the poor solubility and low diffusion coefficient of CO<sub>2</sub> in aqueous solutions, ECR current densities are usually limited to be less than 30 mA cm<sup>-2</sup> in conventional H-cells. This limitation can be overcome by using a flow reactor which can also shorten the diffusion path for the ECR. Virtually, high current densities exceeding 100 mA cm<sup>-2</sup> were easily achieved in a flow cell with 1.0 M aqueous KOH as the electrolyte. Note that the ECR performance over CuO@ZrO<sub>2</sub> invariably surpassed bare CuO. The overall ECR FE is higher than 67.0% throughout the geometric current density regime from 50 to 300 mA cm<sup>-2</sup>, approaching 85.4% at 250 mA cm<sup>-2</sup> (Fig. 5f). In particular, at this high current density, an impressive FE of 54.7 ± 1.1% for C<sub>2</sub>H<sub>4</sub> formation was attained, outperforming many previously reported Cu-based electrocatalysts, as presented in Table S4.

Based on the above experiments and analyses, we infer that the presence of ZrO<sub>2</sub> and abundant defects in CuO both favor CO<sub>2</sub> adsorption and activation to yield more \*CO formation. Higher \*CO coverage facilitates subsequent hydrogenation (to generate COH\* or CHO\*) and C–C coupling preferably at the sites of Cu<sup>+</sup> on the surface of CuO<sup>14</sup>. Meanwhile, an oxygen vacancy may also promote rapid desorption of \*CH<sub>2</sub>, accelerating the conversion of 2\*CH<sub>2</sub> → C<sub>2</sub>H<sub>4</sub>. Among others, the introduction of ZrO<sub>2</sub> effectively suppressed the

undesired HER.<sup>22,37</sup> The nanopits in CuO may extend the residence time of electrogenerated products (as a result of higher adsorption energy in hole surface than a corresponding planar structure) and/or increase the local pH, thereby improving the C–C coupling probability within the confined space<sup>14</sup>.

To gain mechanistic insight into the enhanced C<sub>2</sub>H<sub>4</sub> formation on CuO@ZrO<sub>2</sub>, we performed DFT modeling (Fig. 6). We calculated the interface between CuO and ZrO<sub>2</sub> by binding a ZrO<sub>2</sub> cluster (Zr<sub>8</sub>O<sub>16</sub>) onto the Cu (111) slab (Fig. 6a and Fig. S13a and b). The variation/trend of the Bader charges on the surface Cu in the presence and absence of ZrO<sub>2</sub> clusters was considered given that the Bader charge qualitatively matches with the oxidation state.<sup>18</sup> It is assumed that the Bader charges of surface Cu in Cu (111), Cu<sub>2</sub>O (111), and CuO (111) correlate with the respective oxidation states of 0, +1, and +2. A linear feature between the Bader charge and oxidation state (Fig. 6b) was acquired. The oxidation state of Cu in CuO@ZrO<sub>2</sub> can thus be derived from the correlation. It is obvious that the oxidation states of Cu at the CuO–ZrO<sub>2</sub> interface fall between that of Cu<sub>2</sub>O and CuO (Fig. 6b), suggesting that the interfacial ZrO<sub>2</sub> cluster altered the oxidation state of adjacent Cu in CuO towards that of Cu<sub>2</sub>O. This matches XPS results (Fig. 1b and c), manifesting the existence of Cu<sup>+</sup> in CuO@ZrO<sub>2</sub>. It can thus be inferred that ZrO<sub>2</sub> plays a central role in stabilizing Cu<sup>+</sup>.

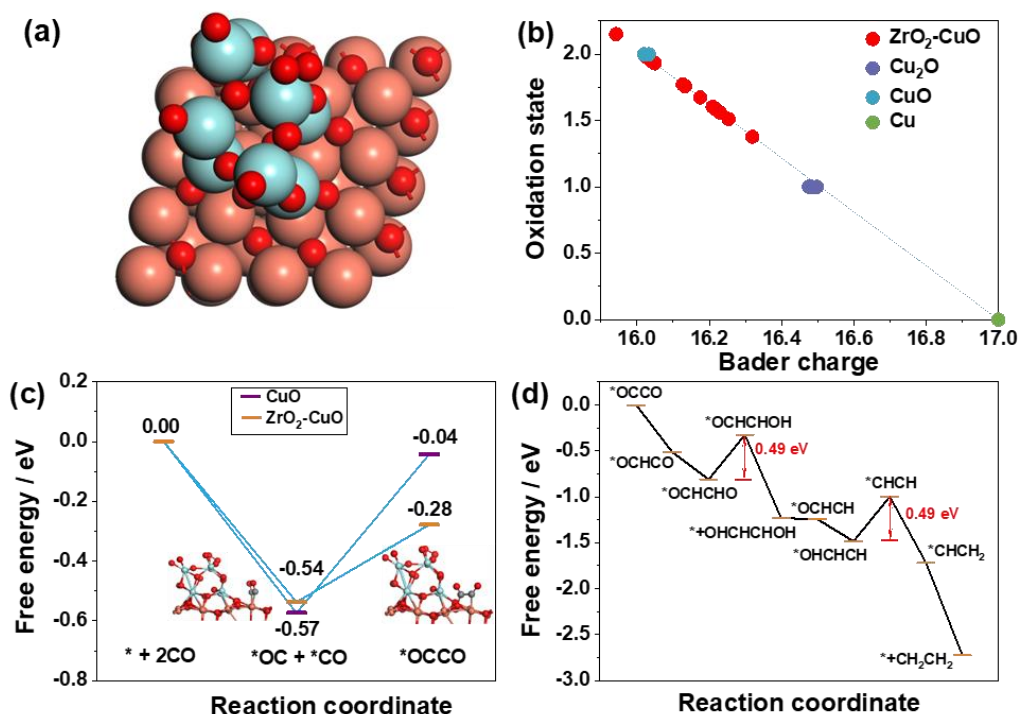


**Fig. 6.** (a) Top view of the optimized geometries of CuO@ZrO<sub>2</sub>. (b) Oxidation states of surface Cu derived by Bader charge investigation. (c) Free energy diagram for \*OCCO production starting from \* + 2CO over pure CuO and CuO@ZrO<sub>2</sub>. (d) Free energy diagram for C<sub>2</sub>H<sub>4</sub> production starting from \*OCCO over CuO@ZrO<sub>2</sub>. All energies are in eV.

We evaluated the capability for C<sub>2</sub> generation by comparison of the energy for dimerization of \*CO into \*CO dimer (\*OCCO), a step that is claimed to be a critical C–C coupling path over copper-based materials. It was calculated that pure CuO and CuO@ZrO<sub>2</sub> both possess a high surface affinity for CO intermediates, which coincides with temperature-programmed desorption of CO (CO-TPD) results (Fig. S14). Note that the dimerization energy of \*CO was substantially lowered (from 0.53 to 0.26 eV) for CuO@ZrO<sub>2</sub> compared to pure CuO (Fig. 6c). In addition, the relative energy of \*CO + \*CO and \*OCCO as opposed to \* + 2CO (g) is –0.54 and –0.28 eV, respectively (Fig. 6c). This supports the hypothesis that the incorporation

of ZrO<sub>2</sub> can effectively promote C<sub>2</sub> formation. Fig. 6d reveals the free energy profile for \*OCCO to C<sub>2</sub>H<sub>4</sub> over CuO@ZrO<sub>2</sub> after considering the possible reaction intermediates for C<sub>2</sub> product generation (Fig. S15). The potential determining step is either \*OCHCHO + (H<sup>+</sup> + e<sup>-</sup>) → \*HCHCHOH or \*OHCHCH + (H<sup>+</sup> + e<sup>-</sup>) → \*CHCH + H<sub>2</sub>O (Fig. 6d). Therefore, at the experimental potential region, CuO@ZrO<sub>2</sub> can boost the overall ECR reactions exothermically to yield C<sub>2</sub>H<sub>4</sub>.

Our results in this work show that the presence of surface Cu<sup>+</sup> stabilized by ZrO<sub>2</sub> significantly enhanced ECR to yield C<sub>2</sub>H<sub>4</sub>. This matches well with many previous reports underpinning the role of Cu<sup>+</sup> during the ECR.<sup>17,18,36</sup> However, in some prior literature,<sup>13,38,39</sup> surface oxide layer without stabilization was observed fully reduced to metallic Cu before the onset potential and Cu<sup>0</sup> was proposed as the main active sites for ECR. We envisage that the exact Cu active sites for ECR may be varied dependent on the catalyst systems. Future study using advanced operando spectroscopy measurements in conjunction with <sup>13</sup>C isotope and rationally designed control experiments by introducing O<sub>2</sub> or O<sub>2</sub>/CO<sub>2</sub> mixture would be more helpful to elucidate the specific active sites and reaction pathways.

## CONCLUSION

To conclude, we have demonstrated that the introduction of ZrO<sub>2</sub> coupled with tuning of nanocavities in CuO greatly facilitates dimerization and protonation of \*CO to yield C<sub>2</sub>H<sub>4</sub> for both electrochemical CO<sub>2</sub> and CO reduction reactions. Such a combined strategy also concurrently inhibits the competitive HER. Modulating the content of ZrO<sub>2</sub> incorporation and defects in CuO allows for fine-tuning of the ECR performance. A significantly higher FE of 47.6 ± 0.5% and cathodic EE of 26.8 ± 0.3% for C<sub>2</sub>H<sub>4</sub> production is achieved over CuO@ZrO<sub>2</sub>

in an H-cell, compared to that of only  $19.7 \pm 1.5\%$  and  $11 \pm 1.9\%$  for bare CuO, respectively. The respective overall FE and FE for C<sub>2</sub>H<sub>4</sub> can be further improved up to  $84.3 \pm 1.6\%$  and  $54.7 \pm 1.1\%$  with a high current density of  $-250 \text{ mA cm}^{-2}$  in a flow reactor. Operando Raman spectroscopy and post-XPS measurements confirmed that ZrO<sub>2</sub> can effectively stabilize Cu<sup>+</sup> against further reduction under CO<sub>2</sub> reduction conditions. The activity of the composite catalyst preserves sufficient stability even after continuous polarization over 12 h. DFT analysis reveals the preferred formation of Cu<sup>+</sup> species (which are likely the main sites for CO<sub>2</sub> adsorption and activation) as well as the lower energy barrier for C–C coupling at the CuO–ZrO<sub>2</sub> interface. This work offers a simple and effective scheme for selective electrochemical reduction of CO<sub>2</sub> and CO to produce C<sub>2</sub>H<sub>4</sub>.

#### ASSOCIATED CONTENT

##### **Supporting Information.**

The Supporting Information is available free of charge on the ACS Publications website at DOI: Experimental section; XRD; wide-survey, O 1s and Zr 3d XPS spectra; H<sub>2</sub>-TPR; SEM and STEM; C<sub>2</sub>H<sub>4</sub> partial geometric current density; scan-rate dependence of cyclic voltammetric stripping; Nyquist plots; the FE of ECR products; Cu 2p XPS after electrolysis; SEM and TEM images after electrolysis; the view of the Cu<sub>2</sub>O and CuO; CO desorption isotherms; the intermediate of the reduction process of CO<sub>2</sub>; summary of C<sub>2</sub>H<sub>4</sub> performance over reported electrocatalysts; the relative percentages of Cu<sup>0</sup>, Cu<sup>+</sup>, and Cu<sup>2+</sup> before and after thermal treatment at different conditions estimated by XPS; the ECR activity optimized by modulating the feeding sequence of the metal salt precursors; summary of C<sub>2</sub>H<sub>4</sub> performance over reported electrocatalysts in flow cell.

## AUTHOR INFORMATION

### Corresponding Author

\*(Z.S.) E-mail: sunzy@mail.buct.edu.cn

### Author Contributions

Z. S. supervised the project. Z. S. and X. L. conceived the idea. X. L. conducted synthesis and electrochemical experiments. S. H. and A. W. R. helped transmission electron microscopy measurements and analysis. L. L. performed DFT calculations. Z. S., X. L. and L. L. wrote the manuscript. A. W. R. polished the language. All authors reviewed the manuscript.

### Notes

The authors declare no competing financial interest.

## ACKNOWLEDGMENT

This work was supported by the National Natural Science Foundation of China (No. 21972010), the Beijing Natural Science Foundation (No. 2192039), and the Foundation of Key Laboratory of Low-Carbon Conversion Science & Engineering, Shanghai Advanced Research Institute, Chinese Academy of Sciences (No. KLLCCSE-201901, SARI, CAS).

## REFERENCES

- (1) Centi, G. Smart catalytic materials for energy transition. *SmartMat* **2020**,1, e1005.
- (2) Hao, L. D.; Sun, Z. Y. Metal oxide-based materials for electrochemical CO<sub>2</sub> reduction. *Acta Phys. -Chim. Sin.* **2021**, 37, 2009033.
- (3) Li, F. W.; Thevenon, A.; Rosas-Hernández, A.; Wang, Z. Y.; Li, Y. L.; Gabardo, C. M., Ozden, A.; Dinh, C. T.; Li, J.; Wang, Y. H.; Edwards, J. P.; Xu, Y.; McCallum, C.; Tao, L. Z. Z.; Liang, Q.; Luo, M. C.; Wang, X.; Li, H.H.; O'Brien, C. P.; Tan, C. S.; Nam, D.H.; Quintero-Bermudez, R.; Zhuang, T. T.; Li, Y. C.; Han, Z. J.; Britt, R. D.; Sinton, D.; Agapie,

- T.; Peters, J. C.; Sargent, E. H. Molecular tuning of CO<sub>2</sub>-to-ethylene conversion. *Nature* **2020**, 577, 509–513.
- (4) Chen, J. M. Carbon neutrality: toward a sustainable future. *The Innovation* **2021**, 2, 100127.
- (5) Tao, H. C.; Fan, Q.; Ma, T.; Liu, S. Z. Gysling, H.; Texter, J.; Guo, F.; Sun, Z. Y.; Two-dimensional materials for energy conversion and storage. *Prog. Mater. Sci.* **2020**, 111, 100637.
- (6) Li, M. H.; Ma, Y. Y.; Chen, J. Lawrence, R.; Luo, W.; Sacchi, M.; Jiang, W.; Yang, J. P.; Residual chlorine induced cationic active species on a porous copper electrocatalyst for highly stable electrochemical CO<sub>2</sub> reduction to C<sub>2+</sub>. *Angew. Chem. Int. Ed.* **2021**, 133, 11588–11594.
- (7) Yan, C. C.; Lin, L.; Wang, G. X.; Bao, X. H. Transition metal-nitrogen sites for electrochemical carbon dioxide reduction reaction. *Chin. J. Catal.* **2019**, 40, 23–27.
- (8) Li, M. H.; Wang, H. F.; Luo, W.; Sherrell, P. C.; Chen, J.; Yang, J. P. Heterogeneous single-atom catalysts for electrochemical CO<sub>2</sub> reduction reaction. *Adv. Mater.* **2020**, 32, 2001848.
- (9) Li, G. D.; Qin, Y. J.; Wu, Y.; Pei, L.; Hu, Q.; Yang, H. P.; Zhang, Q. L.; Liu, J. H.; He, C. X. Nitrogen and sulfur dual-doped high-surface-area hollow carbon nanospheres for efficient CO<sub>2</sub> reduction. *Chin. J. Catal.* **2020**, 41, 830–838.
- (10) Yang, D. X.; Zhu, Q. G.; Han, B. X. Electroreduction of CO<sub>2</sub> in ionic liquid-based electrolytes. *The Innovation* **2020**, 1, 100016.
- (11) Yang, Y.; Zhang, Y.; Hu, J. S.; Wan, L. J. Progress in the mechanisms and materials for CO<sub>2</sub> electroreduction toward C<sub>2+</sub> products. *Acta Phys. -Chim. Sin.* **2020**, 36, 1906085.
- (12) Nitopi, S.; Bertheussen, E.; Scott, S. B.; Liu, X. Y.; Engstfeld, A. K.; Horch, S.; Seger, B.; Stephens, I. E. L.; Chan, K.; Hahn, C.; Norskov, J. K.; Jaramillo, T. F.; Chorkendorff, I. Progress and perspectives of electrochemical CO<sub>2</sub> reduction on copper in aqueous electrolyte. *Chem. Rev.* **2019**, 119, 7610–7672.
- (13) Lee, S. H.; Lin, J. C.; Farmand, M.; Landers, A. T.; Feaster, J. T.; Acosta, J. E.; Beeman, J. W.; Ye, Y. F.; Yano, J. K.; Mehta, A.; Davis, R. C.; Jaramillo, T. S.; Hahn, C.; Drisdell, W. S. Oxidation state and surface reconstruction of Cu under CO<sub>2</sub> reduction conditions from in situ X-ray characterization. *J. Am. Chem. Soc.* **2021**, 143, 588–592.

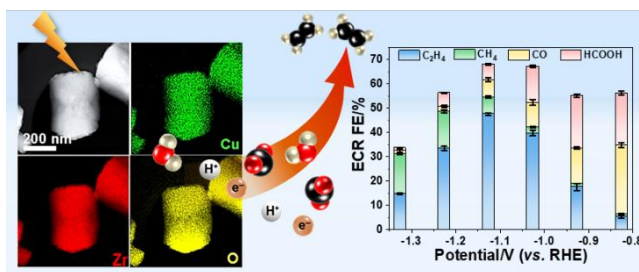


- (14) Jiang, Y. Q.; Choi, C.; Hong, S.; Chu, S. L.; Wu, T. S.; Soo, Y. L.; Hao, L. D.; Jung, Y. S.; Sun, Z. Y. Enhanced electrochemical CO<sub>2</sub> reduction to ethylene over CuO by synergistically tuning oxygen vacancies and metal doping. *Cell Rep. Phys. Sci.* **2021**, 2, 100356.
- (15) Song, Y. F.; Junqueira, J.; Sikdar, N.; Öhl, D.; Dieckhöfer, S.; Quast, T.; Seisel, S.; Masa, J.; Andronesco, C.; Schuhmann, W. B-Cu-Zn gas diffusion electrodes for CO<sub>2</sub> electroreduction to C<sub>2+</sub> products at high current densities. *Angew. Chem. Int. Ed.* **2021**, 60, 9135–9141.
- (16) Li, Y. C.; Wang, Z. Y.; Yuan, T. G.; Nam, D. H.; Luo, M. C.; Wicks, J.; Chen, B.; Li, J.; Li, F. W.; de Arquer, F.; Wang, Y.; Dinh, C. T.; Voznyy, O.; Sinton, D.; Sargent, E. H. Binding site diversity promotes CO<sub>2</sub> electroreduction to ethanol. *J. Am. Chem. Soc.* **2019**, 141, 8584–8591.
- (17) Wu, Y. A.; McNulty, I.; Liu, C.; Lau, K. C.; Liu, Q.; Paulikas, A. P.; Sun, C. J.; Cai, Z. H.; Guest, J. R.; Ren, Y.; Stamenkovic, V.; Curtiss, L.; Liu, Y. Z.; Rajh, T. Facet-dependent active sites of a single Cu<sub>2</sub>O particle photocatalyst for CO<sub>2</sub> reduction to methanol. *Nat. Energy* **2019**, 4, 957–968.
- (18) Chu, S. L.; Yan, X. P.; Choi, C.; Hong, S.; Robertson, A. W.; Masa, J.; Han, B. X.; Jung, Y. S.; Sun, Z. Y. Stabilization of Cu<sup>+</sup> by tuning a CuO–CeO<sub>2</sub> interface for selective electrochemical CO<sub>2</sub> reduction to ethylene. *Green Chem.* **2020**, 22, 6540–6546.
- (19) Luc, W.; Fu, X. B.; Shi, J. J.; Lv, J. J.; Jouny, M.; Ko, B. H.; Xu, Y. B.; Tu, Q.; Hu, X. B.; Wu, J. S.; Yue, Q.; Liu, Y. Y.; Jiao, F.; Kang, Y. J. Two-dimensional copper nanosheets for electrochemical reduction of carbon monoxide to acetate. *Nat. Catal.* **2019**, 2, 423–430.
- (20) Wakerley, D.; Lamaison, S.; Ozanam, F.; Menguy, N.; Mercier, D.; Marcus, P.; Fontecave, M.; Mougél, V. Bio-inspired hydrophobicity promotes CO<sub>2</sub> reduction on a Cu surface. *Nat. Mater.* **2019**, 18, 1222–1227.
- (21) Hua, W.; Sun, H. H.; Xu, F.; Wang, J. G. A review and perspective on molybdenum-based electrocatalysts for hydrogen evolution reaction. *Rare Met.* **2020**, 39, 335–351.
- (22) Nitopi, S.; Bertheussen, E.; Scott, S. B.; Liu, X. Y.; Engstfeld, A. K.; Horch, S.; Seger, B.; Stephens, I.; Chan, K.; Hahn, C.; Nørskov, J. K.; Jaramillo, T. F.; Chorkendorff, I. Progress and perspectives of electrochemical CO<sub>2</sub> reduction on copper in aqueous electrolyte. *Chem. Rev.* **2019**, 119, 7610–7672.

- (23) Soloveichik, G. Electrochemical synthesis of ammonia as a potential alternative to the Haber–Bosch process. *Nat. Catal.* **2019**, 2, 377–380.
- (24) Wang, J. L.; Tan, H. Y.; Zhu, Y. P.; Chu, H.; Chen, H. M. Linking the dynamic chemical state of catalysts with the product profile of electrocatalytic CO<sub>2</sub> reduction. *Angew. Chem. Int. Ed.* **2021**, 133, 17394–17407.
- (25) Zhao, C. M.; Luo, G.; Liu, X. K.; Zhang, W.; Li, Z. J.; Xu, Q.; Zhang, Q. H.; Wang, H. J.; Li, D. M.; Zhou, F. Y.; Qu, Y. T.; Han, X.; Zhu, Z. Z.; Wu, G.; Wang, J.; Zhu, J. F.; Yao, T.; Li, Y. F.; Bouwmeester, H. J. M.; Wu, Y. In situ topotactic transformation of an interstitial alloy for CO electroreduction. *Adv. Mater.* **2020**, 32, 2002382.
- (26) Zhong, D. Z.; Zhao, Z. J.; Zhao, Q.; Cheng, D. F.; Liu, B.; Zhang, G.; Deng, W. Y.; Dong, H.; Zhang, L.; Li, J. K.; Li, J. P.; Gong, J. L. Coupling of Cu (100) and (110) facets promotes carbon dioxide conversion to hydrocarbons and alcohols. *Angew. Chem. Int. Ed.* **2021**, 60, 4879–4885.
- (27) Geng, Z.; Kong, X.; Chen, W.; Su, H.; Liu, Y.; Cai, F.; Wang, G.; Zeng, J. Oxygen vacancies in ZnO nanosheets enhance CO<sub>2</sub> electrochemical reduction to CO. *Angew. Chem. Int. Ed.* **2018**, 57, 6054–6059.
- (28) Xia, J. J.; Guo, H. R.; Cheng, M. Z.; Chen, C. Y.; Wang, M. K.; Xiang, Y.; Li, T. S.; Traversa, E. Electrospun zirconia nanofibers for enhancing the electrochemical synthesis of ammonia by artificial nitrogen fixation. *J. Mater. Chem. A* **2021**, 9, 2145–2151.
- (29) Goda, M. N.; Abdelhamid, H. N.; Said, A. E. A. Zirconium oxide sulfate-carbon (ZrOSO<sub>4</sub>@C) derived from carbonized UiO-66 for selective production of dimethyl ether. *ACS Appl. Mater. Interfaces* **2020**, 12, 646–653.
- (30) Huo, H.; Wang, J.; Fan, Q. K.; Hu, Y. J.; Yang, J. Cu-MOFs derived porous Cu nanoribbons with strengthened electric field for selective CO<sub>2</sub> electroreduction to C<sub>2+</sub> fuels. *Adv. Energy Mater.* **2021**, 11, 2102447.
- (31) Wu, Y. H.; Chen, C. J.; Yan, X. P.; Sun, X. F.; Zhu, Q. G.; Li, P. S.; Li, Y. M.; Liu, S. J.; Ma, J. Y.; Huang, Y. Y.; Han, B. X. Boosting CO<sub>2</sub> electroreduction over a cadmium single-atom catalyst by tuning of the axial coordination structure. *Angew. Chem. Int. Ed.* **2021**, 60, 20803.

- (32) Li, Y. Z.; Wei, B.; Zhu, M. H.; Chen, J. C.; Jiang, Q. K.; Yang, B.; Hou, Y.; Lei, L. C.; Li, Z. J.; Zhang, R. F.; Lu, Y. Y. Synergistic effect of atomically dispersed Ni–Zn pair sites for enhanced CO<sub>2</sub> electroreduction. *Adv. Mater.* **2021**, 33, 2102212.
- (33) Zhang, X.; Li, J. C.; Li, Y. Y.; Jung, Y. H.; Kuang, Y. K.; Zhu, G. Z.; Liang, Y. Y.; Dai, H. J. Selective and high current CO<sub>2</sub> electro-reduction to multicarbon products in near-neutral KCl electrolytes. *J. Am. Chem. Soc.* **2021**, 143, 3245–3255.
- (34) Huang, J. F.; Mensi, M.; Oveisi, E.; Mantella, V.; Buonsanti, R. Structural sensitivities in bimetallic catalysts for electrochemical CO<sub>2</sub> reduction revealed by Ag–Cu nanodimers. *J. Am. Chem. Soc.* **2019**, 141, 2490–2499.
- (35) Altaf, N.; Liang, S. Y.; Huang, L.; Wang, Q. Electro-derived Cu-Cu<sub>2</sub>O nanocluster from LDH for stable and selective C<sub>2</sub> hydrocarbons production from CO<sub>2</sub> electrochemical reduction. *J. Energy Chem.* **2020**, 48, 169–180.
- (36) Yang, P. -P.; Zhang, X. -L.; Gao, F. -Y.; Zheng, Y. -R.; Niu, Z. -Z.; Yu, X. -X.; Liu, R.; Wu, Z. -Z.; Qin, S.; Chi, L. -P.; Duan, Y.; Ma, T.; Zheng, X. -S.; Zhu, J. -F.; Wang, H. -J.; Gao, M. -R.; Yu, S. -H. Protecting copper oxidation state via intermediate confinement for selective CO<sub>2</sub> electroreduction to C<sub>2+</sub> fuels. *J. Am. Chem. Soc.* **2020**, 142, 6400–6408.
- (37) Shen, H.; Choi, C.; Masa, J.; Li, X.; Qiu, J.; Jung, Y.; Sun, Z. Electrochemical ammonia synthesis: mechanistic understanding and catalyst design. *Chem* **2021**, 7, 1708–1754.
- (38) Lee, S. H.; Sullivan, I.; Larson, D. M.; Liu, G.; Toma, F. M.; Xiang, C.; Drisdell, W. S. Correlating oxidation state and surface area to activity from operando studies of copper CO electroreduction catalysts in a gas-fed device. *ACS Catal.* **2020**, 10, 14, 8000–8011.
- (39) Mandal, L.; Yang, K. R.; Motapothula, M. R.; Ren, D.; Lobaccaro, P.; Patra, A.; Sherburne, M.; Batista, V. S.; Yeo, B. S.; Ager, J. W.; Martin, J.; Venkatesan, T. Investigating the role of copper oxide in electrochemical CO<sub>2</sub> reduction in real time. *ACS Appl. Mater. Interfaces* **2018**, 10, 8574–8584.

## For Table of Contents Use Only



We demonstrate synergistic electrolysis of CO<sub>2</sub> and CO to C<sub>2</sub>H<sub>4</sub> by concurrently tuning nanocavities and the interface of CuO with ZrO<sub>2</sub>.